RSC Advances

PAPER

View Article Online
View Journal | View Issue

Cite this: *RSC Adv.*, 2018, **8**, 20764

Enhanced thermoelectric properties of hydrothermally synthesized $Bi_{0.88-x}Zn_xSb_{0.12}$ nanoalloys below the semiconductor–semimetal transition temperature

Ahmad Gharleghi,[ab] Roy-Hung Hung,[a] Zong-Ren Yang,[a] Rasoul Malekfar[b] and Chia-Jyi Liu*[a]

Received 5th May 2018
Accepted 29th May 2018

DOI: 10.1039/c8ra03858a

rsc.li/rsc-advances

$Bi_{0.88-x}Zn_xSb_{0.12}$ alloys with $x = 0.00$, 0.05, 0.10, and 0.15 were prepared using hydrothermal synthesis in combination with evacuating-and-encapsulating sintering. The effects of partial Zn substitution for Bi and different sintering temperatures on the thermoelectric properties of $Bi_{0.88-x}Zn_xSb_{0.12}$ alloys were investigated between 25 K and 425 K. Both the electrical conductivity and absolute thermopower are enhanced for the set of alloys sintered at 250 °C. The maximum power factor of 57.60 μW cm^{-1} K^{-2} is attained for the $x = 0.05$ alloy sintered at 250 °C. As compared with Zn-free $Bi_{0.88}Sb_{0.12}$, both the total thermal conductivity and lattice component are reduced upon Zn doping. Bipolar conduction is observed in both electronic and thermal transport. The maximum zT of 0.47 is attained at 275 K for the $x = 0.05$ alloy sintered at 250 °C.

1. Introduction

Thermoelectric technology provides possibility for direct conversion of solar heat or waste heat into electricity using the Seebeck effect. The efficiency (η_G) of a thermoelectric generator (TEG), $\eta_G = \frac{T_H - T_C}{T_H} \frac{\sqrt{1+zT}-1}{\sqrt{1+zT}+\frac{T_C}{T_H}}$, depends mainly on two parameters: the dimensionless figure-of-merit (zT) of a material of which the integrated segments are made and the temperature difference ($T_H - T_C$) across the hot (T_H) and cold (T_C) sides of the module.[1,2] Recent efforts of producing high zT materials have led to significant enhancement of the efficiency of TEG modules.[3,4] For instance, the heat conversion efficiency of 2.1 watts per square centimeter *via* nanostructured alloys of half-Heusler is recently reported.[3] Although TEG modules are beneficial to energy conversion purposes in a variety of technologies, achieving larger zT magnitudes from cost-effective materials would further widen the horizons of this technology. On the other hand, advancing construction techniques would increase the flexibility of an individual module to operate at high temperature gradients. Various property enhancement strategies for raising zT of potential TE materials beyond traditional and current magnitudes are progressively reported.[5–10] Optimization of the electrical conductivity (σ), thermopower (α) and total thermal conductivity ($\kappa = \kappa_c + \kappa_l$) is required to enhance the thermoelectric figure-of-merit, *i.e.*, $zT = \sigma\alpha^2T/(\kappa_c + \kappa_l)$. Previous reports suggest that the electrical conductivity and thermopower of a thermoelectric material could be enhanced *via* tuning the electronic band structure in order to increase the band degeneracy *via* doping and/or compositing.[5,11] In addition, nanostructuring is widely practiced to reduce the lattice component of the total thermal conductivity.[12–15] Synergetic nanocompositing using appropriate inclusions to produce endotaxially embedded additives could facilitate phonon scattering mechanism with less deterioration to the electronic transport of charge carriers.[15–18] Furthermore, thermopower enhancement *via* nanostructuring could be achieved especially for a system possessing high density of carriers.[19] Locally formed nano grains would induce electrical barriers that filter low energy charge carriers.[18,20] Developing strategies for high zT values in conjunction with searching for new promising materials are the ongoing research efforts in thermoelectrics.[15,21,22] Among potential thermoelectric materials, $Bi_{1-x}Sb_x$ alloys have also attracted great research attention both due to its relatively high zT and their interesting physical properties as topological insulators.[3,23,24] $Bi_{1-x}Sb_x$ alloys crystallize in an A_7 type crystal structure, a rhombohedral lattice with space group $R\bar{3}m$ (#166) and 6 atoms per hexagonal unit cell.[25,26] Similar to single crystals of Bi and Sb elements, $Bi_{1-x}Sb_x$ alloys also possess semimetal characteristics as a result of valance and conduction bands overlapping for $0.00 \leq x \leq 0.05$.[27,28] It is also found that $Bi_{1-x}Sb_x$ undergoes

[a]*Department of Physics, National Changhua University of Education, Changhua 500, Taiwan. E-mail: liucj@cc.ncue.edu.tw*

[b]*Department of Physics, Faculty of Basic Science, Tarbiat Modares University, Tehran, I. R. Iran*

a semimetal–semiconductor transition at high Sb content and displays semiconducting characteristics for $0.07 < x \leq 0.22$.[28,29] $Bi_{1-x}Sb_x$ single crystals with $0.05 < x \leq 0.40$ are n-type intrinsic narrow band-gap semiconductors with $E_g \cong 0.014$ eV between 30 and 300 K.[27–29] Based on the experimental results, a larger power factor could be attained at low Sb concentrations in $Bi_{1-x}Sb_x$ single crystals.[27] It is known that zT of $Bi_{1-x}Sb_x$ alloys is highly anisotropic and very sensitive to the composition stoichiometry.[3,24] Earlier studies of $Bi_{1-x}Sb_x$ nanowires predicted their potential of displaying relatively high zT magnitudes at low temperatures.[30] Recently, the influence of applied magnetic field on the thermoelectric properties of $Bi_{90}Sb_{10}$ alloy is investigated. It is found that both the electrical resistivity and thermopower increase in the presence of an applied magnetic field.[23] Moreover, it is found that a high zT value of 1.35 could be achieved for a slightly Te-doped (on the order of 10^{-4} at%) $Bi_{1-x}Sb_x$ single crystal under an applied magnetic field of 0.5 T.[31]

In this work we have investigated the effects of both partial Zn substitution for Bi and sintering temperature on the thermoelectric properties of $Bi_{0.88-x}Zn_xSb_{0.12}$ alloys. $Bi_{0.88-x}Zn_xSb_{0.12}$ alloys were fabricated by a combination of hydrothermal synthesis and evacuated-and-encapsulated sintering. The structural/microstructural analyses and transport property measurements are performed for all the samples. We find that partial Zn substitution results in significant enhancement of thermoelectric power factor and reduction of the lattice thermal conductivity.

2. Experimental procedure

Hydrothermal methods were used to synthesize $Bi_{0.88-x}Zn_xSb_{0.12}$ alloys ($x = 0.00$, 0.05, 0.10, and 0.15). Sb, $BiCl_3$ and $ZnCl_2$ were quantitatively mixed to have the molar ratio of (Bi + Zn)/Sb = 0.88/0.12. In a typical reaction, 8 mmol of ethylenediaminetetraacetic acid (EDTA, $C_{10}H_{16}N_2O_8$), 64 mmol of NaOH and 40 mmol of $NaBH_4$ together with 150 mL of deionized (DI) water were used. The weighed chemicals were poured into a Teflon cup containing DI water followed by stirring at room temperature. After stirring for 30 min, the Teflon cup containing the solution was loaded into an autoclave and sealed. The autoclave was then heated up to 170 °C at the rate of 2.5 °C min^{-1} and kept for 48 h. The resulting precipitate was then washed sequentially using DI water and ethanol followed by drying in an oven at 80 °C for 2 h. The crystal structure of the dried powder was examined using a powder X-ray diffractometer (Shimadzu 6000, Fe Kα radiation). The phase pure powders were cold pressed into cuboids. The obtained cuboids were loaded into a Pyrex tube and evacuated using a diffusion pump to reach 10^{-5} to 10^{-6} torr and then sealed. The evacuated-and-encapsulated ampoule containing the cuboids was then heated in a box furnace with the rate of 2.5 °C min^{-1}. Different sintering temperatures were adopted for the same duration of 10 h. The lattice constants were refined for all the samples. The morphology of as-sintered samples was characterized by a field emission scanning electron microscope (FE-SEM; JEOL JSM-7800F Prime).

The standard four-probe and steady-state techniques were used for simultaneously measuring electrical resistivity and thermopower, respectively, between 25 K and 425 K. The temperature difference between hot and cold ends of the sample was measured using a type E differential thermocouple.[32] The temperature gradient between both ends of the sample is produced using a heater connected to one end of the sample. Thermal conductivity measurements were carried out *via* sandwiching a dual spiral sensor between a couple of pelleted samples using the Hot Disk plane source technique.[33,34] In this technique, the dual spiral sensor also acts as a resistance thermometer. A Hot Disk thermal constants analyzer was used to record the time dependent temperature increase measured by the resistance thermometer. The measurements of the electrical resistivity, thermopower, and thermal conductivity have the estimated uncertainty of about ±3%, ±4% and ±5%, respectively. The bulk density of the sintered samples was determined using the Archimedes' method.

3. Results and discussion

Fig. 1 shows the X-ray diffraction (XRD) patterns of as-hydrothermally synthesized powders of $Bi_{0.88-x}Zn_xSb_{0.12}$ alloys with $x = 0.00$, 0.05, 0.10, and 0.15. All the diffraction peaks could be well indexed using the Miller indices (*hkl*) based on a rhombohedral unit cell lattice with the space group $R\bar{3}m$ (#166).[26,35] Except for the $x = 0.15$ sample, all the $Bi_{0.88-x}Zn_xSb_{0.12}$ powders are of single phase (Fig. 1). The impurity peak indicated by asterisks in the XRD pattern of $x = 0.15$ is attributed to the most intense peaks of Sb phase.

The hydrothermally synthesized $Bi_{0.88-x}Zn_xSb_{0.12}$ powders ($x = 0.00$, 0.05, 0.10 and 0.15) were sintered at two different temperatures, *i.e.*, 170 °C and 250 °C, for the same duration of 10 h. Fig. 2a and b show the XRD patterns of $Bi_{0.88-x}Zn_xSb_{0.12}$ sintered at 170 °C and 250 °C, respectively. All the diffraction peaks of the as-sintered $Bi_{0.88-x}Zn_xSb_{0.12}$ samples are well indexed with the Miller indices. It should be noted that the $x = 0.15$ sample turns into a single phase upon sintering either at

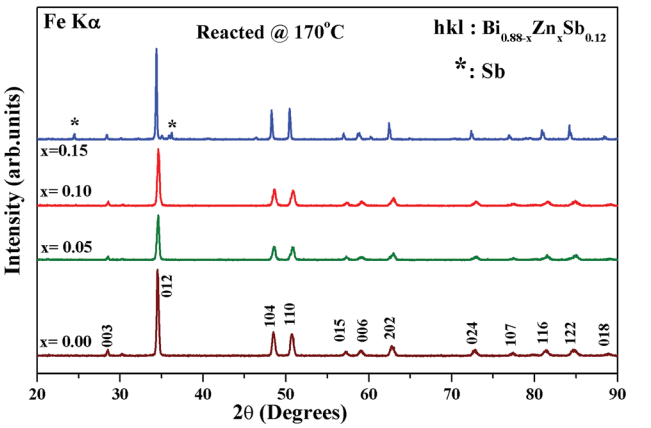

Fig. 1 XRD patterns of hydrothermally synthesized powders of $Bi_{0.88-x}Zn_xSb_{0.12}$ alloys with $x = 0.00$, 0.05, 0.10 and 0.15. The (*hkl*) indicates Miller indices based on a rhombohedral unit cell lattice with the space group $R\bar{3}m$ (#166). The asterisks symbol (*) denotes the most intense peaks of Sb phase.

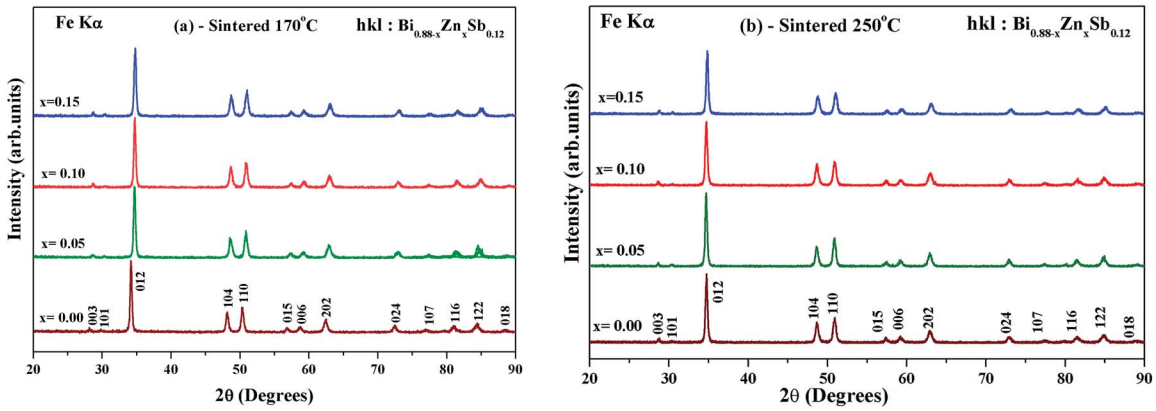

Fig. 2 Powder XRD patterns of $Bi_{0.88-x}Zn_xSb_{0.12}$ alloys with $x = 0.00$, 0.05, 0.10, and 0.15 sintered (a) at 170 °C and (b) 250 °C for the same duration of time of 10 h.

170 °C and 250 °C. Table 1 shows the refined lattice constants of all the $Bi_{0.88-x}Zn_xSb_{0.12}$ alloys. The lattice constants in both set of samples shrink with increasing Zn content. This is associated with a smaller effective ionic radius of Zn^{2+} (0.74 Å for coordination number = 6) than that of Bi^{3+} (1.03 Å for coordination number = 6).[36,37]

The relative bulk density of $Bi_{0.88-x}Zn_xSb_{0.12}$ alloys falls between 94–99% and 95–99% of the theoretical density for samples sintered at 170 °C and 250 °C, respectively (Table 1). The porosity of $Bi_{0.88-x}Zn_xSb_{0.12}$ alloys seems to decrease with increasing Zn content based on the density measurements.

Fig. 3 illustrates the FE-SEM images of the fractured surface of the $x = 0.00$ and 0.05 samples sintered at 170 °C (Fig. 3a and b) and 250 °C (Fig. 3c and d), respectively. One can readily see that the microstructures are irregularly multi-sized aggregates with porosity. The unevenly distribution of porosity within the present structures is apparent from the micrographs.

Fig. 4a and b illustrates the temperature dependence of the electrical conductivity for $Bi_{0.88-x}Zn_xSb_{0.12}$ alloys ($x = 0.00$, 0.05, 0.10, and 0.15) sintered at 170 °C and 250 °C, respectively, between 25 K and 425 K. Except for the $x = 0.15$ sample sintered at 170 °C, it can be readily seen that the electrical conductivity exhibits a hump behavior and is nonmetal-like below 300–325 K. As compared with the $x = 0.00$ sample, the electrical conductivity increases for the $x = 0.05$ and 0.10 alloys for all the investigated temperatures, while it decreases for $x = 0.15$ for most of the investigated temperatures. For the same Zn content, the electrical conductivity is larger for the set of alloys sintered at 250 °C than that sintered at 170 °C. For both sets of samples, the electrical conductivity is largest for the $x = 0.10$ alloy with its maximum occurring at 300 K. Similar temperature dependence of the electrical conductivity is also observed for $Bi_{0.88}Sb_{0.12}$ alloys synthesized *via* quenching and annealing procedures.[38,39] The temperature dependence of the electrical conductivity for the $x = 0.15$ alloy is similar to that of $Bi_{0.85}Sb_{0.15}$ fabricated using mechanical alloying combined with high-pressure sintering procedure.[40] The temperature dependence of the electrical conductivity for $Bi_{0.88-x}Zn_xSb_{0.12}$ is expected to be closely associated with the relative shifting of the T, L_s, and L_a bands.[41,42] The downturn of electrical conductivity above 300–325 K could be attributed to the semiconductor–semimetal transition, which will be discussed in the following section.

Fig. 5a and b displays $\ln(\sigma)$ *versus* T^{-1} for $Bi_{0.88-x}Zn_xSb_{0.12}$ alloys with $x = 0.00$, 0.05, 0.10, and 0.15 sintered at 170 °C and

Table 1 Physical properties of $Bi_{0.88-x}Zn_xSb_{0.12}$ alloys with $x = 0.00$, 0.05, 0.10, and 0.15 synthesized at 170 °C for 48 h followed by sintering for 10 h at 170 °C and 250 °C, respectively. Average grain size is estimated using Scherrer's formula

		$Bi_{0.88-x}Zn_xSb_{0.12}$			
Property	Unit	$x = 0.00$	$x = 0.05$	$x = 0.10$	$x = 0.15$
Lattice constant, $a = b$, c (sintered @ 170 °C)	Å	4.5535(2), 11.8034(9)	4.5064(2), 11.7609(9)	4.5011(2), 11.7595(8)	4.4980(1), 11.7517(5)
Lattice constant, $a = b$, c (sintered @ 250 °C)	Å	4.5126(2), 11.7655(9)	4.5045(2), 11.7710(9)	4.5008(2), 11.7698(8)	4.4906(1), 11.7295(5)
Relative density (sintered @ 170 °C)	%	93.98	94.65	97.92	99.39
Relative density (sintered @ 250 °C)	%	95.36	95.64	97.99	99.21
Average grain size (sintered @ 170 °C)	nm	58	48	49	45
Average grain size (sintered @ 250 °C)	nm	59	67	53	55

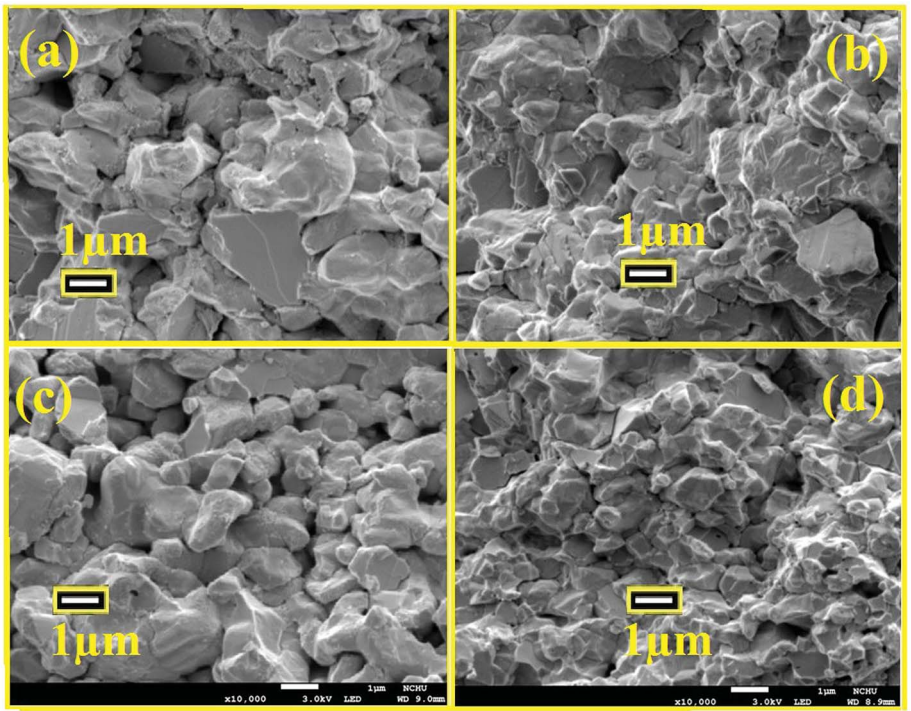

Fig. 3 The FE-SEM micrographs of the fractured surface for $Bi_{0.88-x}Zn_xSb_{0.12}$ sintered at 170 °C with (a) $x = 0.00$ and (b) $x = 0.05$; $Bi_{0.88-x}Zn_xSb_{0.12}$ sintered at 250 °C with (c) $x = 0.00$ and (d) $x = 0.05$.

250 °C, respectively. The corresponding transition temperature of each alloy is shown in the plot. The semiconductor–semimetal transition temperature is lower for the alloys sintered at 250 °C than at 170 °C. Moreover, the transition temperature for the $x = 0.00$ alloy is ~400 K, while the $x = 0.15$ alloy displays no transition within the investigated temperature region (Fig. 5a). For the set of alloys sintered at 250 °C, the semiconductor–semimetal transition temperature varies between 300 K ($x = 0.05$ and 0.10) and 326 K ($x = 0.00$ and 0.15).

Furthermore, to explore the influence of Zn dopants on the electronic structure of $Bi_{0.88-x}Zn_xSb_{0.12}$ alloys, the electrical conductivity curves are fitted using the Arrhenius relationship, $\sigma = \sigma_0 e^{-\frac{E_g}{2k_B T}}$, in the activated conduction region, where σ is the electrical conductivity, σ_0 the pre-exponential factor, E_g the energy band gap, k_B the Boltzmann's constant, and T the absolute temperature. Fig. 6a and b shows the fitted curves of $\ln(\sigma)$ *versus* T^{-1} for $Bi_{0.88-x}Zn_xSb_{0.12}$ alloys with $x = 0.00$, 0.05, 0.10, and 0.15 sintered at 170 °C and 250 °C, respectively. Obviously, the Arrhenius relationship could only be satisfied for limited temperature intervals below the semiconductor–semimetal transition temperature. The magnitudes of E_g are estimated from the slop of the fitted curves and indicated in the

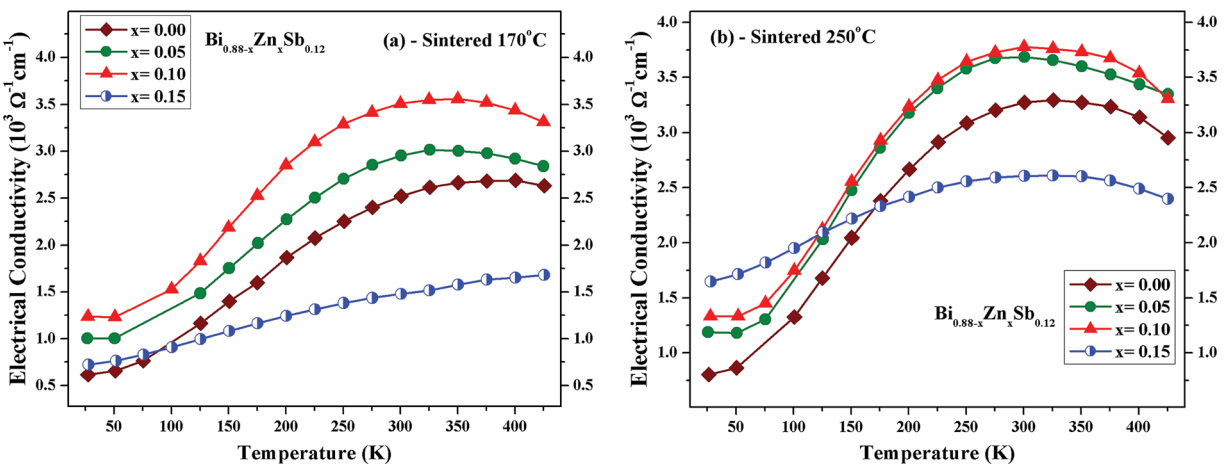

Fig. 4 Temperature dependence of the electrical conductivity of $Bi_{0.88-x}Zn_xSb_{0.12}$ alloys ($x = 0.00$, 0.05, 0.10, and 0.15) sintered at (a) 170 °C and (b) 250 °C.

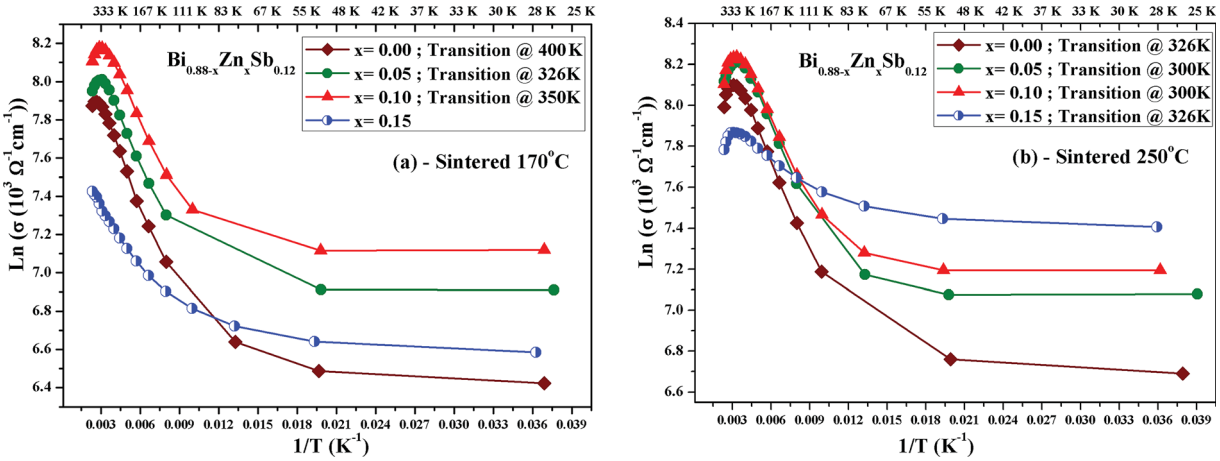

Fig. 5 Plot of ln(σ) *versus* T^{-1} for $Bi_{0.88-x}Zn_xSb_{0.12}$ alloys with $x = 0.00$, 0.05, 0.10, and 0.15, sintered (a) at 170 °C and (b) at 250 °C.

vicinity of the fitting lines. The magnitudes of E_g for both set of alloys display no systematic trend with Zn content. As shown in Fig. 6a, the magnitude of E_g for the set of alloys sintered at 170 °C is slightly larger than that for the set of alloys sintered at 250 °C. Among $Bi_{0.88-x}Zn_xSb_{0.12}$, the $x = 0.15$ alloy has the narrowest band gap. The magnitude of E_g is comparable with that of nanosized $Bi_{1-x}Sb_x$ alloys for $0.12 \leq x \leq 30$.[41] Moreover, the diminished electrical conductivity of the $x = 0.15$ alloys could be partly attributed to the increased offset between the light hole and heavy hole bands. This effect would weaken the contribution of heavy bands to the electronic properties.[41,42] Similar scenario is provided for explaining the influence of valence band offset on electronic properties of p-type $PbTe_{1-x}Se_x$ alloys.[11]

Fig. 7a and b shows the temperature dependence of thermopower for $Bi_{0.88-x}Zn_xSb_{0.12}$ alloys with $x = 0.00$, 0.05, 0.10, and 0.15 sintered at 170 °C and 250 °C, respectively. The thermopower of all the samples is negative indicating that electrons are the majority charge carriers. In addition, the thermopower curves in both set of alloys display similar temperature dependence for the same Zn content x. The temperature dependences of thermopower for $Bi_{0.88-x}Zn_xSb_{0.12}$ alloys are similar to that of $Bi_{0.85}Sb_{0.15}$ fabricated using melt-spinning combined with spark plasma sintering and of a $Bi_{88}Sb_{12}$ single crystal grown by a modified Bridgman method.[35,43] As shown in Fig. 8a, the absolute thermopower for the set of samples sintered at 170 °C increases with increasing temperature between 25 and 150 K, while it keeps increasing even up to 275 K for $x = 0.15$. Besides, the thermopowers of all the samples only show small differences and display similar temperature dependence between 275 K and 425 K. Among the set of alloys sintered at 250 °C, the $x = 0.05$ alloy exhibits the largest absolute thermopowers between 75 and 375 K. It is noted that the variation of thermopower with temperature for the $x = 0.15$ alloy is slower than other alloys, which resembles that of $Bi_{0.85}Sb_{0.15}$ fabricated using mechanical alloying combined with high-pressure sintering.[40]

Fig. 8 shows the thermoelectric power factor ($\sigma\alpha^2$) of $Bi_{0.88-x}Zn_xSb_{0.12}$ alloys with $x = 0.00$, 0.05, 0.10, and 0.15 as a function of temperature from 50 K to 425 K. It can be readily seen that the set of alloys sintered at 250 °C (Fig. 8b) has larger power factors than those for the set of alloys sintered at 170 °C (Fig. 8a). For the former, the $x = 0.05$ alloy reaches the maximum power factor of 57.6 μW cm^{-1} K^{-2} at 175 K; for the latter, the $x = 0.10$ alloy reaches the maximum power factor of 40.8 μW cm^{-1} K^{-2} at 225 K.

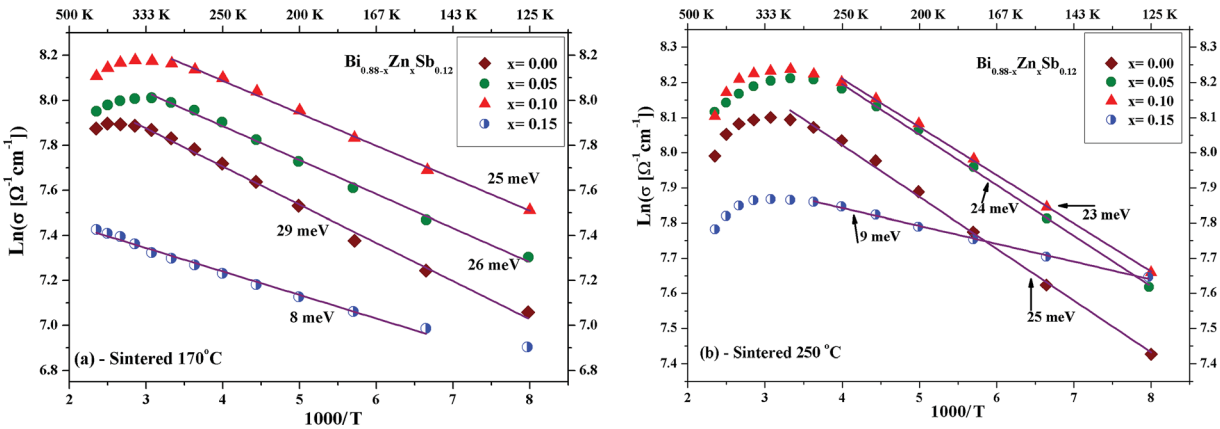

Fig. 6 Curve Fitting of ln(σ) *versus* T^{-1} for $Bi_{0.88-x}Zn_xSb_{0.12}$ alloys ($x = 0.00$, 0.05, 0.10, and 0.15) sintered (a) at 170 °C and (b) at 250 °C. Reasonable linearity could be obtained above 125 K. Energy band gap is given for each curve.

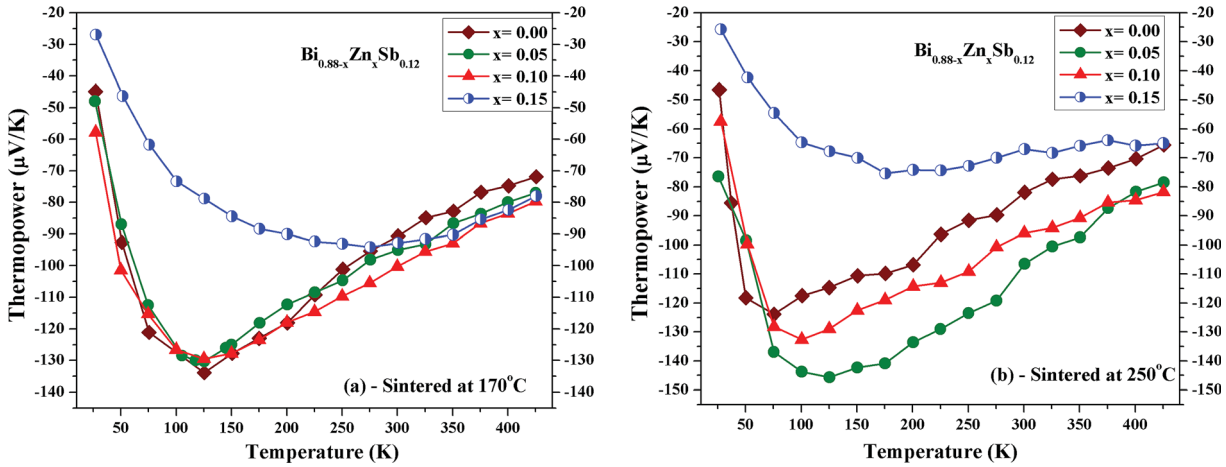

Fig. 7 Temperature dependence of thermopower of $Bi_{0.88-x}Zn_xSb_{0.12}$ alloys with $x = 0.00$, 0.05, 0.10, and 0.15 sintered at (a) 170 °C and (b) 250 °C for the same duration of 10 h.

Fig. 9 displays the temperature dependence of the total thermal conductivity (κ) of $Bi_{0.88-x}Zn_xSb_{0.12}$ alloys with $x = 0.00$, 0.05, 0.10, and 0.15 between 125 K and 300 K. The $x = 0.00$ alloy has the highest κ in both set of alloys, which however is still lower than that of a polycrystalline sample of $Bi_{88}Sb_{12}$ fabricated using evacuating-and-encapsulating heating followed by water quenching.[43] It can be readily seen that κ decreases upon partial replacement of Zn for Bi in both set of alloys. For the set of alloys sintered at 170 °C, the $x = 0.05$ alloy has the κ of 2.31 W m^{-1} K^{-1} at 125 K and 2.72 W m^{-1} K^{-1} at 300 K, while the $x = 0.00$ alloy has the κ of 3.35 W m^{-1} K^{-1} at 125 K and 3.67 W m^{-1} K^{-1} at 300 K. For the set of alloys sintered at 250 °C, the $x = 0.15$ alloy has the κ of 2.68 W m^{-1} K^{-1} at 125 K and 3.06 W m^{-1} K^{-1} at 300 K, while the $x = 0.00$ alloy has the κ of 3.21 W m^{-1} K^{-1} at 125 K and 3.48 W m^{-1} K^{-1} at 300 K.

To derive the contribution of charge carriers to the total thermal conductivity, the electronic component ($\kappa_e + \kappa_{bp}$) are separately estimated. The Wiedemann–Franz law is applied to estimate $\kappa_e = \sigma LT$, where $L = 2.44 \times 10^{-8}$ W Ω K^{-2} denotes the Lorenz number and σ the measured electrical conductivity at a given temperature T. The upturn behavior of κ can be attributed to bipolar contribution to the electronic thermal conductivity. Hence, we consider the bipolar contribution of the thermal conductivity κ_{bp}, which can be expressed using the following equation[44,45]

$$\kappa_{bp} = \frac{3L\sigma T}{4\pi^2}\left(\frac{E_g}{k_B T} + 4\right), \quad (1)$$

where E_g is calculated using the Arrhenius relationship. The combined results ($\kappa_e + \kappa_{bp}$) for electronic contribution to the thermal conductivity are illustrated in Fig. 10a and b for both sets of $Bi_{0.88-x}Zn_xSb_{0.12}$ alloys sintered at 170 °C and 250 °C, respectively. The calculated results indicate that the electronic contribution is relatively small at low temperatures, and yet it increases with increasing temperature.

The lattice phonon component (κ_L) is obtained by subtracting the electronic contribution from the total thermal conductivity ($\kappa_L = \kappa - \kappa_e - \kappa_{bp}$). The results are plotted in Fig. 11 for both set of alloys sintered at 170 °C and 250 °C, respectively. One can readily see that the κ_L of alloys sintered at 170 °C is

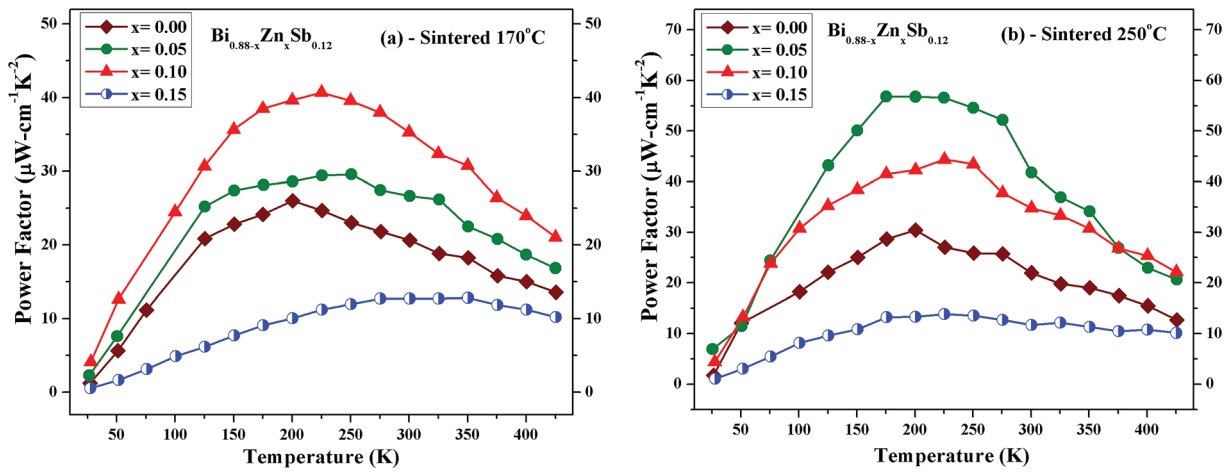

Fig. 8 Temperature dependence of power factor ($\sigma\alpha^2$) of $Bi_{0.88-x}Zn_xSb_{0.12}$ alloys with $x = 0.00$, 0.05, 0.10, and 0.15 sintered at (a) 170 °C and (b) 250 °C for the same duration of 10 h.

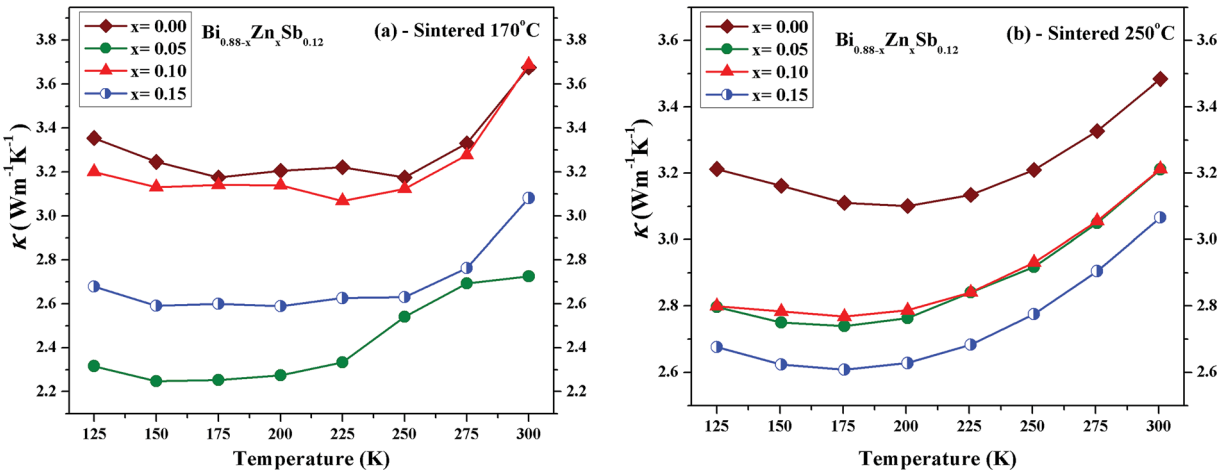

Fig. 9 Temperature dependence of the total thermal conductivity (κ) of $Bi_{0.88-x}Zn_xSb_{0.12}$ alloy with $x = 0.00$, 0.05, 0.10, and 0.15 sintered at (a) 170 °C and (b) 250 °C for the same duration of 10 h.

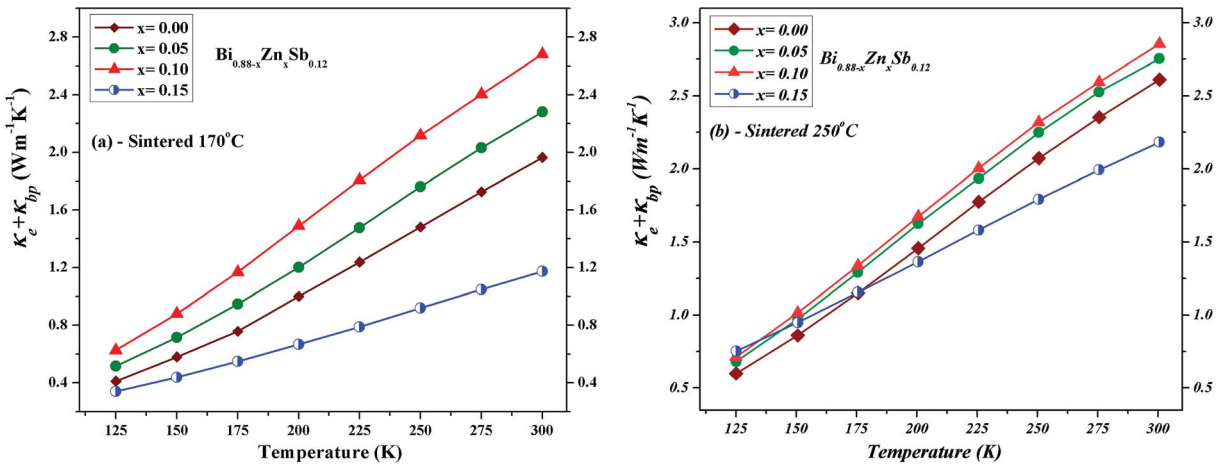

Fig. 10 Temperature dependence of the electronic contribution ($\kappa_e + \kappa_{bp}$) for $Bi_{0.88-x}Zn_xSb_{0.12}$ alloys with $x = 0.00$, 0.05, 0.10, and 0.15 sintered at (a) 170 °C and (b) 250 °C for the same duration of 10 h.

slightly lower than that sintered at 250 °C because the latter might have better crystallinity. The magnitude of κ_L decreases upon Zn doping for both set of alloys and dominates at low temperatures but becomes smaller than electronic contribution as the temperature approaches 300 K. Point defects can account for the reduction of κ_L upon Zn doping due to the mass

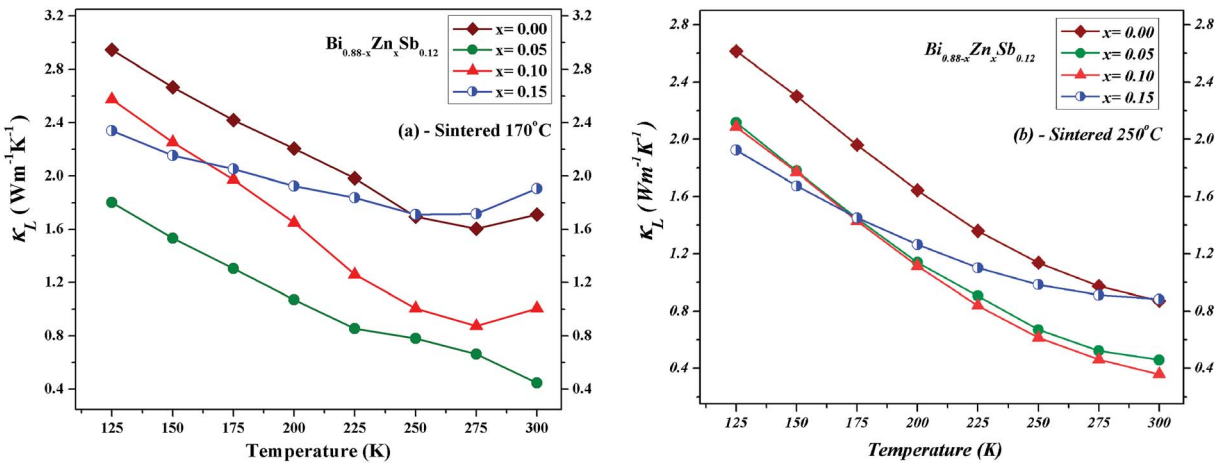

Fig. 11 Temperature dependence of the lattice contribution κ_L for $Bi_{0.88-x}Zn_xSb_{0.12}$ alloys with $x = 0.00$, 0.05, 0.10 and 0.15 measured at $125 \leq T/K \leq 300$, sintered at (a) 170 °C and (b) 250 °C for the same duration of 10 h.

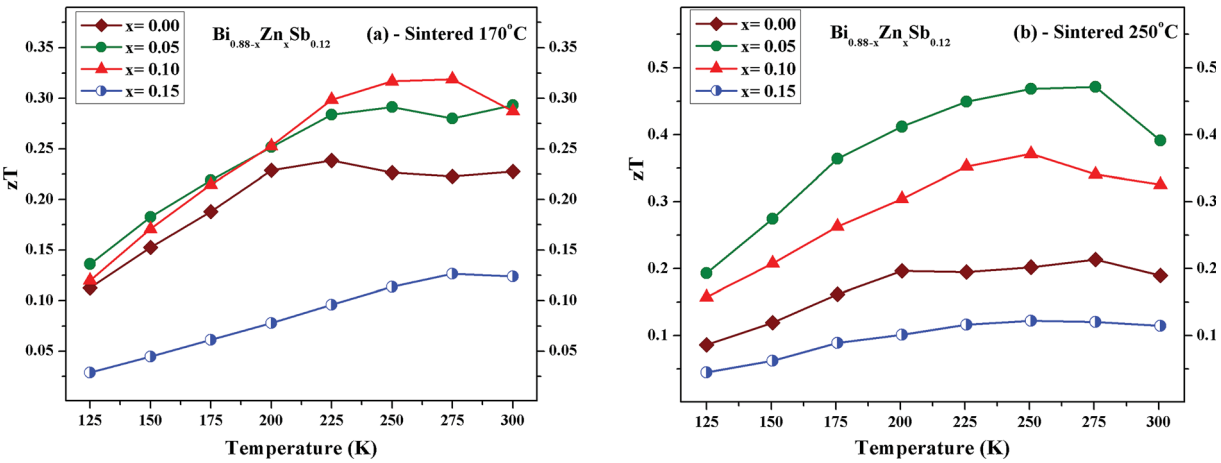

Fig. 12 Temperature dependence of thermoelectric figure-of-merit (zT) of $Bi_{0.88-x}Zn_xSb_{0.12}$ alloys with $x = 0.00$, 0.05, 0.10 and 0.15 between 125 K to 300 K, that were sintered (a) at 170 °C and (b) at 250 °C for the same duration of 10 h.

difference between Zn and Bi.[33,46,47] Moreover, the smallest κ_L occurs at the Zn doping content of $x = 0.05$ and $x = 0.10$ sintered at 170 °C and 250 °C, respectively. As the temperature increases up to 300 K, unlike the $x = 0.05$ and 0.10 alloys, the κ_L of the $x = 0.15$ alloy gradually approach that of the $x = 0.00$ alloy.

Fig. 12 displays the temperature dependence of zT for $Bi_{0.88-x}Zn_xSb_{0.12}$ alloys with $x = 0.00$, 0.05, 0.10, and 0.15. The maximum zT value is 0.32 and 0.47 both occurring at 275 K for $x = 0.10$ alloy sintered at 170 °C and the $x = 0.05$ alloy sintered at 250 °C, respectively. The value of $zT = 0.47$ is comparable or even higher as compared with other reports for Bi–Sb alloys in the absence of magnetic field.[23,24,27] Moreover, the maximum zT value is smaller than 0.25 for the $x = 0.00$ alloy in both set of samples, while it is enhanced as compared with that of mechanically alloyed $Bi_{88}Sb_{12}$.[48] For comparison with other similar bismuth antimony alloy systems, a maximum value of $zT \approx 0.23$ was attained for Sn-doped $(Bi_{85}Sb_{15})_{1-x}Sn_x$ with $x = 0.00$ fabricated using pressureless sintering techniques;[49] a maximum value of $zT \approx 0.26$ was attained at 260 K for $(Bi_{85}Sb_{15})_{1-x}Pb_x$ with $x = 0.00$ fabricated using mechanical alloying in combination with pressureless sintering.[50] For $Bi_{85}Sb_{13}Nb_2$ fabricated using high-press sintering, a maximum of $zT = 0.36$ was attained at 200 K.[40] It should be noted that $zT > 1$ could be attained for Bi–Sb–Te alloys around room temperature.[51,52]

4. Conclusions

A series of $Bi_{0.88-x}Zn_xSb_{0.12}$ alloys with $x = 0.00$, 0.05, 0.10, and 0.15 was fabricated *via* hydrothermal synthesis in combination with evacuating-and-encapsulated sintering. The effects of partially replacing Bi by Zn and different sintering temperatures on electronic and thermal transport of $Bi_{0.88-x}Zn_xSb_{0.12}$ alloys were investigated. The XRD patterns of as-synthesized $Bi_{0.88-x}Zn_xSb_{0.12}$ alloys indicate that $Bi_{0.88-x}Zn_xSb_{0.12}$ with $x = 0.00$, 0.05, and 0.10 are of single phase, while the $x = 0.15$ alloy contains an impurity phase of Sb. The lattice constant refinements show the shrinkage of the lattice constants, which confirms the partial replacement of Zn on Bi sites.

The downturn temperature dependence of the electrical conductivity around room temperature is attributed to semiconductor–semimetal transition, which is observed for all the alloys except the $x = 0.15$ alloy sintered at 170 °C. For the effects of Zn doping, the power factors are enhanced for all $Bi_{0.88-x}Zn_xSb_{0.12}$ alloys, except that for the $x = 0.15$ alloy. For the effects of sintering temperature, larger power factors could be attained for alloys sintered at 250 °C as compared to 170 °C. The largest power factor of 57.60 μW cm^{-1} K^{-2} is attained for the $x = 0.05$ alloy sintered at 250 °C. The total thermal conductivity in both sets of the $Bi_{0.88-x}Zn_xSb_{0.12}$ alloys is reduced as compared with the Zn-free $Bi_{0.88}Sb_{0.12}$ alloy.

Bipolar transport plays a significant role both in the electronic and thermal transport. It is found that the electronic thermal conductivity dominates the heat conduction in the vicinity of 273 K. The largest zT of 0.47 is attained at 275 K for the $x = 0.05$ alloy sintered at 250 °C.

Conflicts of interest

There are no conflicts of interest to declare.

Acknowledgements

This work was supported by Ministry of Science and Technology of Taiwan under the Grant No. 104-2112-M-018-002-MY3. Ahmad Gharleghi would like to express thanks for the post-doctoral fellowship sponsored by MOST during the stay in Taiwan and by Iran National Elite Association.

References

1 D. M. Rowe, *Thermoelectrics Handbook: Macro to Nano*, CRC/Taylor & Francis, Boca Raton, 2006.
2 H. J. Goldsmid, *Thermoelectric refrigeration*, Plenum Press, New York, 1964.
3 Y. Zhang, X. Wang, M. Cleary, L. Schoensee, N. Kempf and J. Richardson, *Appl. Therm. Eng.*, 2016, **96**, 83–87.

4 M. Jaworski, M. Bednarczyk and M. Czachor, *Appl. Therm. Eng.*, 2016, **96**, 527–533.
5 T. Fu, X. Yue, H. Wu, C. Fu, T. Zhu, X. Liu, L. Hu, P. Ying, J. He and X. Zhao, *Journal of Materiomics*, 2016, **2**, 141–149.
6 A. Mehdizadeh Dehkordi, M. Zebarjadi, J. He and T. M. Tritt, *Mater. Sci. Eng., R*, 2015, **97**, 1–22.
7 P. Sun, B. Wei, J. Zhang, J. M. Tomczak, A. M. Strydom, M. Søndergaard, B. B. Iversen and F. Steglich, *Nat. Commun.*, 2015, **6**, 7475.
8 X. Zhang, C. Chang, Y. Zhou and L.-D. Zhao, *Materials*, 2017, **10**, 198.
9 W.-T. Chiu, C.-L. Chen and Y.-Y. Chen, *Sci. Rep.*, 2016, **6**, 23143.
10 J. G. Park and Y. H. Lee, *Curr. Appl. Phys.*, 2016, **16**, 1202–1215.
11 Y. Pei, X. Shi, A. LaLonde, H. Wang, L. Chen and G. J. Snyder, *Nature*, 2011, **473**, 66–69.
12 D.-B. Zhang, H.-Z. Li, B.-P. Zhang, D.-D. Liang and M. Xia, *RSC Adv.*, 2017, **7**, 10855.
13 J.-F. Li, W.-S. Liu, L.-D. Zhao and M. Zhou, *NPG Asia Mater.*, 2010, **2**, 152–158.
14 G. Joshi, H. Lee, Y. Lan, X. Wang, G. Zhu, D. Wang, R. W. Gould, D. C. Cuff, M. Y. Tang, M. S. Dresselhaus, G. Chen and Z. Ren, *Nano Lett.*, 2008, **8**, 4670–4674.
15 K. Biswas, J. He, I. D. Blum, C.-I. Wu, T. P. Hogan, D. N. Seidman, V. P. Dravid and M. G. Kanatzidis, *Nature*, 2012, **489**, 414–418.
16 Z.-H. Ge, D. Song, X. Chong, F. Zheng, L. Jin, X. Qian, L. Zheng, R. E. Dunin-Borkowski, P. Qin, J. Feng and L.-D. Zhao, *J. Am. Chem. Soc.*, 2017, **139**, 9714–9720.
17 K. Biswas, J. He, Q. Zhang, G. Wang, C. Uher, V. P. Dravid and M. G. Kanatzidis, *Nat. Chem.*, 2011, **3**, 160–166.
18 J.-H. Bahk, Z. Bian and A. Shakouri, *Phys. Rev. B: Condens. Matter Mater. Phys.*, 2013, **87**, 075204.
19 Y.-M. Lin and M. S. Dresselhaus, *Phys. Rev. B: Condens. Matter Mater. Phys.*, 2003, **68**, 075304.
20 J. Martin, L. Wang, L. Chen and G. S. Nolas, *Phys. Rev. B: Condens. Matter Mater. Phys.*, 2009, **79**, 115311.
21 L.-D. Zhao, C. Chang, G. Tan and M. G. Kanatzidis, *Energy Environ. Sci.*, 2016, **9**, 3044–3060.
22 Z. Liu, H. Geng, J. Mao, J. Shuai, R. He, C. Wang, W. Cai, J. Sui and Z. Ren, *J. Mater. Chem. A*, 2016, **4**, 16834–16840.
23 M. Murata, A. Yamamoto, Y. Hasegawa and T. Komine, *J. Electron. Mater.*, 2016, **45**(3), 1875–1885.
24 H. Zhang, J. S. Son, J. Jang, J.-S. Lee, W.-L. Ong, J. A. Malen and D. V. Talapin, *ACS Nano*, 2013, **7**(11), 10296–10306.
25 M. Hansen and K. Anderko, *Constitution of binary alloys*, McGraw-Hill Book Company, New York, 1958, pp. 332–334.
26 R. J. Cava, H. Ji, M. K. Fuccillo, Q. D. Gibson and Y. S. Hor, *J. Mater. Chem. C*, 2013, **1**, 3176–3189.
27 G. E. Smith and R. Wolfe, *J. Appl. Phys.*, 1962, **33**(3), 841–846.
28 Y.-M. Lin, O. Rabin, S. B. Cronin, J. Y. Ying and M. S. Dresselhaus, *Appl. Phys. Lett.*, 2002, **81**(13), 2403–2405.
29 B. Lenoir, A. Dauscher, X. Devaux, Y. I. Ravich, R. Martin-Lopez, H. Scherrer and S. Scherrer, in *Proceedings of the 15th international conference on thermoelectrics*, IEEE, Pasadena, CA, Piscataway, NJ, 1996, p. 1.
30 O. Rabina, Y.-M. Lin and M. S. Dresselhaus, *Appl. Phys. Lett.*, 2001, **79**(1), 81–83.
31 V. S. Zemskov, A. D. Belaya, U. S. Beluy and G. N. Kozhemyakin, *J. Cryst. Growth*, 2000, **212**, 161–166.
32 A. Gharleghi and C.-J. Liu, *J. Alloys Compd.*, 2014, **592**, 277–282.
33 A. Gharleghi, Y.-H. Chu, F.-H. Lin, Z.-R. Yang, Y.-H. Pai and C.-J. Liu, *ACS Appl. Mater. Interfaces*, 2016, **8**, 5205–5215.
34 C.-J. Liu, H.-C. Lai, Y.-L. Liu and L.-R. Chen, *J. Mater. Chem.*, 2012, **22**, 4825–4831.
35 T. Luo, S. Wang, H. Li and X. Tang, *Intermetallics*, 2013, **32**, 96–102.
36 X.-Y. Zha, L.-J. Gao, H.-C. Bai, J.-L. Wang and S.-F. Wang, *Chin. Phys. B*, 2017, **26**(10), 107202.
37 D. M. Freik, S. I. Mudryi, I. V. Gorichok, V. V. Prokopiv, O. M. Matkivsky, I. O. Arsenjuk, O. S. Krynytsky and V. M. Bojchyk, *Ukr. J. Phys.*, 2016, **61**, 155–159.
38 K. Malik, D. Das, S. K. Neogi, A. K. Deb, A. Dasgupta, S. Bandyopadhyay and A. Banerjee, *J. Phys. Chem. Solids*, 2016, **91**, 7–12.
39 H. Kitagawa, H. Noguchi, T. Kiyabu, M. Itoh and Y. Noda, *J. Phys. Chem. Solids*, 2004, **65**, 1223–1227.
40 C. Song, R. Huang, M. Zhou, L. Gong and L. Li, *J. Phys. Chem. Solids*, 2010, **71**, 999–1003.
41 C. H. Will, M. T. Elm, P. J. Klar, B. Landschreiber, E. Günes and S. Schlecht, *J. Appl. Phys.*, 2013, **114**, 193707.
42 A. L. Jain, *Phys. Rev.*, 1959, **114**(6), 1518.
43 C. M. Orovets, A. M. Chamoire, H. Jin, B. Wiendlocha and J. P. Heremans, *J. Electron. Mater.*, 2012, **41**, 1648–1652.
44 A. R. Regel, I. A. Smirnov and E. V. Shadrichev, *J. Non-Cryst. Solids*, 1972, **8–10**, 266–271.
45 J. He, M. G. Kanatzidis and V. P. Dravid, *Mater. Today*, 2013, **16**, 166–176.
46 P. G. Klemens, *Proc. Phys. Soc., London, Sect. A*, 1955, **68**, 1113–1128.
47 J. Callaway and H. C. von Baeyer, *Phys. Rev.*, 1960, **120**, 1149–1154.
48 R. Martin-Lopez, A. Dauscher, H. Scherrer, J. Hejtmanek, H. Kenzari and B. Lenoir, *Appl. Phys. A*, 1999, **68**, 597–602.
49 Z. Chen, M. Zhou, R. Huang, C. Huang, C. Song, Y. Zhou and L. Li, *J. Electron. Mater.*, 2012, **41**(6), 1725–1729.
50 Z. Chen, M. Zhou, R. J. Huang, C. M. Song, Y. Zhou and L. F. Li, *J. Alloys Compd.*, 2012, **511**, 85–89.
51 B. Poudel, Q. Hao, Y. Ma, Y. Lan, A. Minnich, B. Yu, X. Yan, D. Wang, A. Muto, D. Vashaee, X. Chen, J. Liu, M. S. Dresselhaus, G. Chen and Z. Ren, *Science*, 2008, **320**, 634–638.
52 Y. Luo, J. Yang, Q. Jiang, W. Li, D. Zhang, Z. Zhou, Y. Cheng, Y. Ren and X. He, *Acta Mater.*, 2017, **127**, 185–191.